Spatiotemporal flow instabilities of wormlike micellar solutions in rectangular microchannels

S. J. Haward, F. J. Galindo-Rosales, P. Ballesta, and M. A. Alves

Articles you may be interested in
Shear banding in time-dependent flows of polymers and wormlike micelles
J. Rheol. **58**, 103 (2014); 10.1122/1.4842155

Role of shear-thinning on the dynamics of rinsing flow by an impinging jet
Phys. Fluids **24**, 093102 (2012); 10.1063/1.4752765

Passive flow control in microdevices using thermally responsive polymer solutions
Phys. Fluids **18**, 053103 (2006); 10.1063/1.2204077

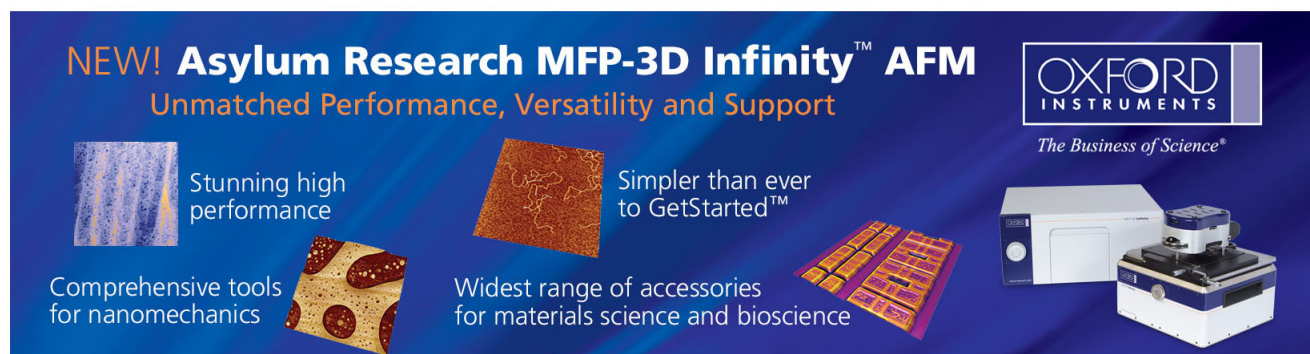Investigation of shear-banding structure in wormlike micellar solution by point-wise flow-induced birefringence measurements
J. Rheol. **49**, 537 (2005); 10.1122/1.1849179

Transition to shear banding in pipe and Couette flow of wormlike micellar solutions
J. Rheol. **43**, 897 (1999); 10.1122/1.551008

Spatiotemporal flow instabilities of wormlike micellar solutions in rectangular microchannels

S. J. Haward,[a] F. J. Galindo-Rosales, P. Ballesta, and M. A. Alves

Departamento de Engenharia Química, Faculdade de Engenharia da Universidade do Porto,
Rua Dr Roberto Frias s/n, 4200-465 Porto, Portugal

Flow velocimetry measurements are made on a non-shear-banding wormlike micellar solution within high-aspect-ratio rectilinear microchannels over a wide range of imposed steady flow rates. At the lowest and highest flow rates tested, Newtonian-like velocity profiles are measured. However, at intermediate flow rates the velocity field never stabilizes on the timescale of the experiments (up to several hours). Here, spatiotemporally dependent "jets" of high velocity fluid are observed to fluctuate within regions of essentially stagnant fluid. The reason for this flow instability remains undetermined, but it has significant consequences for many industrial applications and also for microfluidic rheometry of complex fluids. © 2014 Author(s). All article content, except where otherwise noted, is licensed under a Creative Commons Attribution 3.0 Unported License. [http://dx.doi.org/10.1063/1.4869476]

Wormlike micelles are formed by the self-assembly of surfactant molecules in solution.[1,2] They exist in a dynamic equilibrium with their solvent and for this reason are sometimes referred to as "living polymers." The dynamic breakage and reformation of the micelles confers unique viscoelastic properties to the fluids, which have made them extremely useful in a wide range of applications including inkjet printing, enhanced oil recovery, district heating systems, and as rheology modifiers in countless consumer products.[3–5] In semidilute to concentrated wormlike micellar systems, the rate of micelle breaking and reformation can dominate the characteristic timescale of the fluid (the fast-breaking limit) and in such cases the resulting linear rheological response of the fluid obeys almost ideal Maxwellian behavior described by a single-mode Maxwell-Debye relaxation mechanism.[6,7] For this reason, semidilute wormlike micellar solutions are often considered to be simple model viscoelastic fluids. However, their non-linear rheological behavior (which is far more relevant to any real-world process or application) is anything but simple. Here, a range of poorly understood phenomena are encountered, including shear-banding,[8–12] flow-induced structure formation,[13,14] and elastic and interfacial instabilities.[15–21]

In this Letter, we consider a semidilute wormlike micellar solution formed from 30 mM of the surfactant cetyltrimethyl ammonium bromide (CTAB) in the presence of 240 mM sodium salicylate (NaSal) flowing in a simple high-aspect ratio rectangular rectilinear microchannel. The fluid is seeded with $1\,\mu$m diameter fluorescent particles (volume fraction $\phi \approx 2 \times 10^{-4}$) to enable micro-particle image velocimetry (μ-PIV) measurements, described below. Measurements of the steady shear rheology in a cone-and-plate rotational rheometer at $25\,^{\circ}$C show the fluid is strongly shear-thinning, but does not display the clear plateau of constant stress that is characteristic of shear-banding micellar

fluids (Fig. 1).[8,9] This rheological response is typical of fluids of the particular formulation used here.[22,23] The steady rheology is well described by the Carreau generalized Newtonian fluid (GNF) model

$$\eta(\dot{\gamma}) = \eta_{\infty} + (\eta_0 - \eta_{\infty})\left[1 + (\dot{\gamma}/\dot{\gamma}^*)^2\right]^{(n-1)/2}, \quad (1)$$

where $\eta_{\infty} = 0.07\,\mathrm{Pa\,s}$ is the infinite-shear-rate viscosity, $\eta_0 = 3.3\,\mathrm{Pa\,s}$ is the zero-shear-rate viscosity, $\dot{\gamma}$ is the applied shear rate, $\dot{\gamma}^* = 0.95\,\mathrm{s}^{-1}$ is the characteristic shear rate for the onset of shear-thinning, and $n = 0.28$ is the "power-law exponent" in the shear-thinning region.

The microchannel employed in most of the experiments has a depth $d = 275 \pm 5\,\mu$m in the z-direction and width $w = 2.2$ mm in the y-direction, providing a high aspect ratio $\alpha = w/d = 8$ and a hydraulic diameter $D_h = 2wd/(w + d)$ $= 489\,\mu$m. The total length of the channel in the direction of flow (i.e., the x-direction) is $L = 6$ cm, therefore $L/D_h \approx 123$. We define the origin of coordinates as being at the center of the channel cross-section and at the location of the channel inlet. Two of the side-walls are made from precision $250\,\mu$m-thick steel shim while the remaining two walls are formed from standard glass microscope slides. Bonds between the glass and steel are made using a solvent-resistant epoxy resin with a layer thickness of approximately 12–$15\,\mu$m on each side, top and bottom. The flow inside the channel is driven at controlled volume flow rates $0.00022\,\mu\mathrm{l\,s}^{-1} \leq Q \leq 1\,\mu\mathrm{l\,s}^{-1}$ using a high precision neMESYS syringe pump and Hamilton Gastight syringes. To ensure essentially pulsation-free injection of fluid into the channel, syringe volumes are selected such that required flow rate is achieved by driving the pump at no less than $40\times$ the minimum specified rate. Typically, the pumping rate used corresponds to at least 100 increments-per-second of the pump stepper motor, or more than 2 orders of magnitude greater than the inverse relaxation time of the CTAB solution, $1/\lambda \cong \dot{\gamma}^* = 0.95\,\mathrm{s}^{-1}$. At such high discretization, no feedback between the fluid drive and response is to be

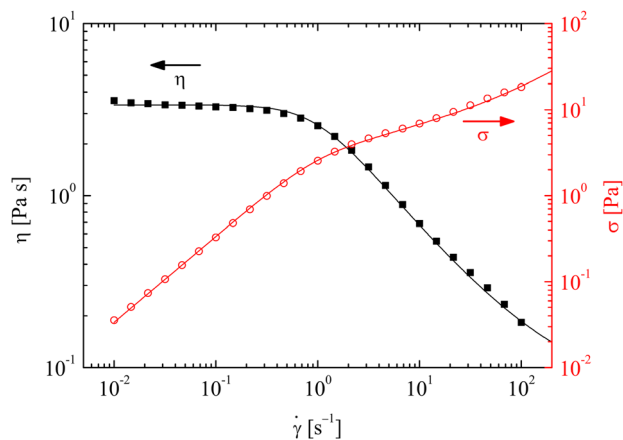[a]Author to whom correspondence should be addressed. Electronic mail: shaward@fe.up.pt.

104, 124101-1

FIG. 1. Steady flow curves of viscosity (η) and shear stress (σ) as a function of the shear rate ($\dot\gamma$) measured for the CTAB test fluid at 25 °C and fitted with the Carreau model (Eq. (1), solid lines).

expected. The average flow velocity inside the channel is given by $U = Q/wd$ and the nominal wall shear rate can be estimated as $\dot\gamma_{wall} \approx 6U/d$. The range of wall shear rates examined in the microchannel experiments is thus $0.01\,\text{s}^{-1} \leq \dot\gamma_{wall} \leq 40\,\text{s}^{-1}$, closely corresponding to the range of shear rates covered in the rotational rheometer (Fig. 1). The Reynolds number in the channel is defined as $\text{Re} = \rho U D_h/\eta(\dot\gamma)$, where $\rho \approx 1000\,\text{kg m}^{-3}$ is the fluid density and the shear-rate-dependent viscosity, $\eta(\dot\gamma)$, is estimated using the nominal wall shear rate in Eq. (1). In all the experiments presented here $\text{Re} < 3 \times 10^{-3}$, thus inertial effects can be disregarded.

The fully-developed flow of the CTAB solution through the rectangular channel is numerically simulated in Matlab (Mathworks, Inc.) by solving the transient Stokes equation using a time marching scheme until convergence is obtained. The fitted Carreau GNF model (Eq. (1)) is used as the constitutive equation for the shear-rate-dependent fluid viscosity. Note that this model accounts only for the shear-thinning and not for any memory effects that might be expected for a micellar solution.

For μ-PIV measurements, the flow channel is placed on the imaging stage of an inverted microscope (Olympus IX83) and a $4\times$ NA = 0.13 objective lens is focused at the center-plane of the channel depth (i.e., at $z = 0$). A diode-pumped pulsed 526.5 nm neodymium-doped yttrium lithium fluoride (Nd:YLF) laser (Litron Lasers LDY300) excites the fluorescent tracer particles in the fluid (Nile Red, Molecular Probes, Invitrogen Ex/Em = 535 nm/575 nm). An epifluorescent filter cube is used to prevent the laser light from reaching the sensor of a high-speed CMOS camera (Phantom Miro M340, Vision Research), which thus only receives the light emitted by the fluorescent particles. An additional $1.9\times$ lens is used to ensure the whole CMOS sensor is illuminated. This system allows instantaneous imaging across the entire channel width. Use of higher magnification, higher NA objectives would increase accuracy, but would require scanning of the focal position across the channel width in order to obtain the complete velocity profile. This would not only slow down the data acquisition, which is not desirable in a potentially time-varying flow field, but would also complicate the subsequent image and data analysis unnecessarily.

Images are captured continuously at rates such that the average frame-by-frame particle displacement is around 3 pixels, which is optimal for subsequent PIV analysis. The analysis is performed using an adaptive cross-correlation PIV algorithm with interrogation areas that reduce from 64×64 to 16×16 pixels, implemented in Dynamic Studio software (Dantec Dynamics). The maximum full-frame acquisition rate of the Phantom Miro CMOS camera is 800 fps (frames-per-second), while the actual acquisition rates used for the experimental measurements are 600 fps at the highest flow rates and proportionally slower at lower imposed flow rates. The adaptive PIV algorithm itself is capable of resolving flow velocity vectors for frame-to-frame pixel displacements of between 0.1 and 20 pixels.

Initial control experiments involve seeding a Newtonian fluid (water) with fluorescent tracer particles and making μ-PIV measurements for Newtonian flow at low Reynolds numbers. In this case, the streamwise velocity profiles measured across the channel width and at the center-plane for various imposed flow rates are self-similar and closely conform to the analytically computed profile (Fig. 2), thus confirming the suitable accuracy of the measurement technique.

Depending upon the imposed flow rate, subsequent experiments with the shear-thinning viscoelastic CTAB solution reveal a sequence of entirely unpredictable spatiotemporally varying velocity profiles (Fig. 3).

At very low flow rates, e.g., $Q = 0.00022\,\mu\text{l s}^{-1}$ (corresponding to a nominal wall shear rate $\dot\gamma_{wall} \approx 0.01\,\text{s}^{-1}$, Fig. 3(a)), the velocity profile across the width of the microchannel is similar to the Newtonian case, is well-described by the Carreau GNF model and remains essentially invariant over long time periods ($>2\,\text{h}$ of observation in this case). However, at intermediate flow rates, the velocity profiles across the channel become quite atypical (Figs. 3(b) and 3(c)). Here, as shown in the example given in Fig. 3(b) ($Q = 0.0555\,\mu\text{l s}^{-1}$, $\dot\gamma_{wall} \approx 2\,\text{s}^{-1}$), in some regions of the channel the fluid can be almost stagnant, with essentially all of the volume being transported along narrow "jet-like" sections. The peak flow velocity within the jet can reach values
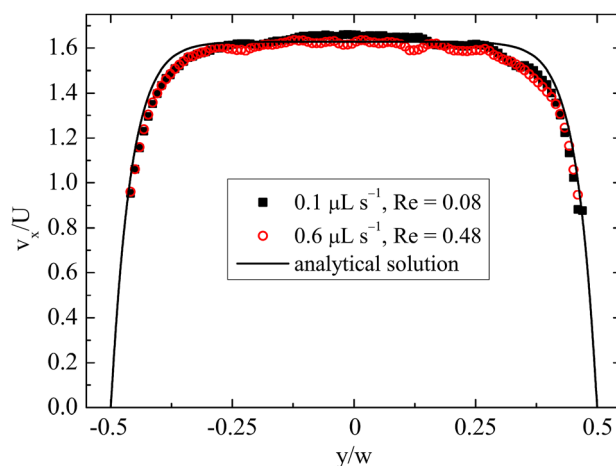

FIG. 2. Results of μ-PIV measurements made at the center-plane of the rectangular microchannel with a Newtonian fluid (water) at low Re, compared with the analytical solution obtained for fully developed laminar Newtonian flow.
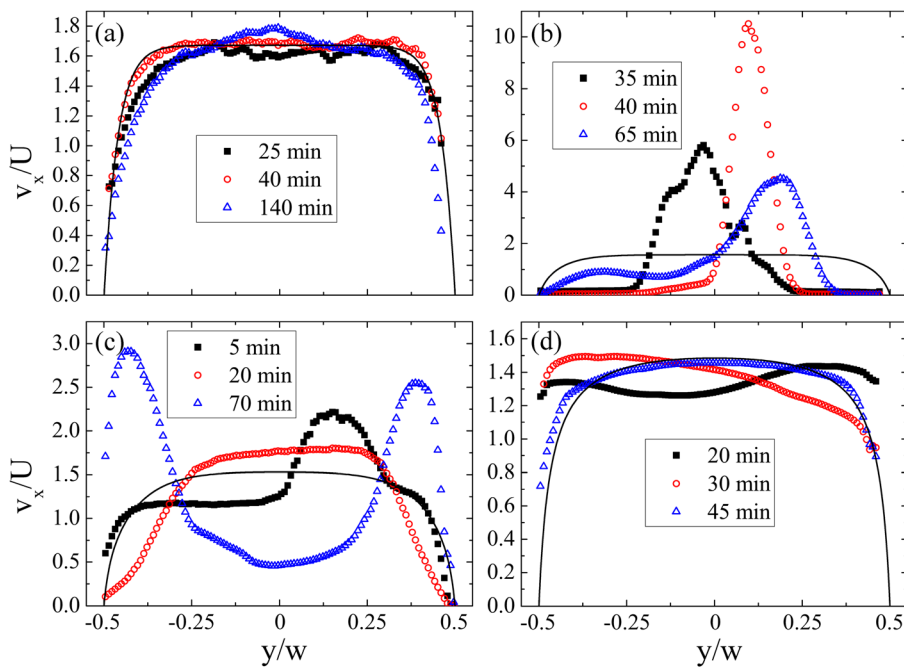
FIG. 3. Velocity profiles measured at the center-plane of the rectangular microchannel with the 30 mM CTAB 240 mM NaSal solution at 25 °C at various flow rates: (a) $Q = 0.00022$ $\mu l\,s^{-1}$, $\dot{\gamma}_{wall} \approx 0.01\,s^{-1}$; (b) $Q = 0.0555\,\mu l\,s^{-1}$, $\dot{\gamma}_{wall} \approx 2\,s^{-1}$; (c) $Q = 0.139\,\mu l\,s^{-1}$, $\dot{\gamma}_{wall} \approx 5\,s^{-1}$; and (d) $Q = 1.0\,\mu l\,s^{-1}$, $\dot{\gamma}_{wall} \approx 36\,s^{-1}$. In each case the solid line represents the numerical prediction of the velocity profile determined using the fit of the Carreau model to the steady shear rheology (see Eq. (1), Fig. 1). The times quoted in the figure legends are the approximate times from the startup of flow at each respective flow rate. Profiles are obtained from approximately 40 mm downstream of the channel inlet.

of up to $v_x/U \approx 10$. The position of the jet and the width of the jet region appear to be metastable, and fluctuate over time periods on the order of minutes, which is much longer than the relaxation time of the fluid ($\lambda \sim 1/\dot{\gamma}^* \approx 1.1\,s$). Experiments have been conducted in which the microchannel is translated along its entire length between the inlet ($x = 0\,mm$) and the outlet ($x \approx 60\,mm$). These high velocity jets can persist for the entire length of the microchannel, only varying slightly in width and position. At this volume flow rate, the average flow velocity in the channel is $U \approx 0.1\,mm\,s^{-1}$, so the nominal transit time for fluid along the length of the channel is $\approx 10\,min$. Fig. 3(c) shows velocity profiles obtained across the channel at various times for a flow rate of $Q = 0.139\,\mu l\,s^{-1}$ ($\dot{\gamma}_{wall} \approx 5\,s^{-1}$). In this particular example, at early times (e.g., 5 min after startup of flow) the profile appears almost plug-like, but with a superimposed high velocity region to the right-hand side of the channel centerline. After 20 min of continuous flow, the flow field looks as though it might be developing towards the expected plug-like profile predicted by the Carreau model. Subsequently, however, an extremely unusual velocity distribution develops in which two high-velocity fluid jets are observed close to the channel side walls and the lowest velocity is measured along the channel centerline. As previously, such velocity distributions appear to be metastable and can remain essentially unaltered for periods spanning many minutes of observation. At the highest flow rate tested ($Q = 1.0\,\mu l\,s^{-1}$, $\dot{\gamma}_{wall} \approx 36\,s^{-1}$), initial fluctuations are observed before the flow velocity distribution approaches the prediction of the Carreau model and subsequently tends to stabilize (Fig. 3(d)). In order to provide confirmation that the jets observed at intermediate flow rates are not due to any pulsation from the syringe pump, experiments have been performed using a range of syringes. For example, at the volume flow rate of $Q = 0.139\,\mu l\,s^{-1}$ ($\dot{\gamma}_{wall} \approx 5\,s^{-1}$, Fig. 3(c)) syringes of 100 μl and 2500 μl have been utilized. At this flow rate, these two syringes require the pump to increment at approximately 2400 and 100 steps-per-second,

respectively. Use of different syringes to drive the flow results in no qualitative difference in the observation of the jets of fluid within the flow channel, indicating that pulsation of the syringe pump is not a causal factor.

Fig. 4 shows a space-time diagram constructed from velocity profiles made across the rectilinear microchannel at a single x-location approximately 40 mm downstream from the channel inlet ($x/w \approx 18$) over a 150 min time period for continuous flow of the CTAB solution at $Q = 0.0555$ $\mu l\,s^{-1}$ ($\dot{\gamma}_{wall} \approx 2\,s^{-1}$). Measurements commence approximately 10 min after the startup of flow and initially appear to show an almost uniform plug-like velocity profile across the channel. However, after approximately 15 min more of observation, the velocity distribution becomes asymmetric, with a velocity peak growing on the left-hand side and a corresponding trough developing to the right-hand side of the channel. Over the subsequent 10–15 min period, the peak velocity shifts towards the right-hand side of the channel and
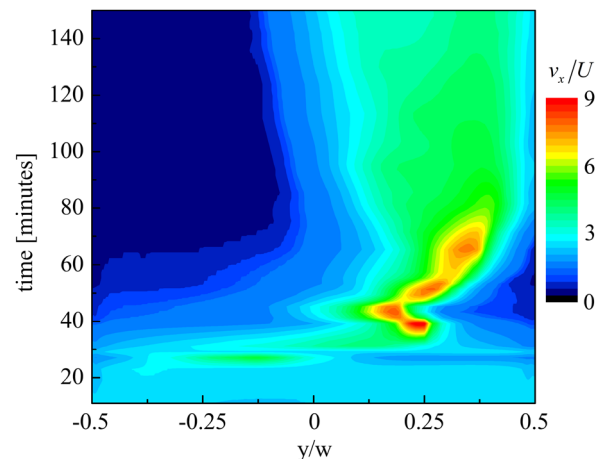

FIG. 4. Space-time diagram formed from μ-PIV measurements made across the rectangular microchannel at a single x-location ($x \approx 40\,mm$) over a 2.5 h time period. The volume flow rate is $Q = 0.0555\,\mu l\,s^{-1}$, providing a nominal wall shear rate $\dot{\gamma}_{wall} \approx 2\,s^{-1}$.
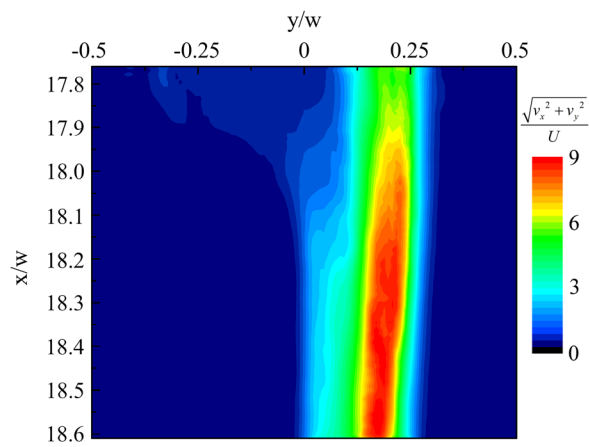
FIG. 5. Instantaneous μ-PIV measurement in the x-y plane over a section of the rectangular microchannel centered on $x \approx 40\,\text{mm}$ ($x/w \approx 18.2$). The flow direction is from top to bottom, the volume flow rate is $Q = 0.0555\,\mu\text{l s}^{-1}$ ($\dot{\gamma}_{wall} \approx 2\,\text{s}^{-1}$) and flow has been imposed for 50 min (Multimedia view) [URL: http://dx.doi.org/10.1063/1.4869476.1].

develops into a very high velocity jet centered at $y/w \approx 0.2$ with a maximum velocity of $v_x/U \approx 9$. Subsequently, the jet shifts first left then right and also gradually reduces in intensity. Finally, after around 70 min a metastable state is achieved in which the flow is concentrated along the right-hand side of the channel with the fluid at the left-hand side being almost stagnant; this state persists with only minor alteration for the remaining 80 min of observation.

Fig. 5 shows an example of a velocity field in the $z = 0$ plane of the microchannel for a case in which a significant spatial variation in velocity is observed along the x-direction. In this example, the flow rate is again $Q = 0.0555$ $\mu\text{l s}^{-1}$ ($\dot{\gamma}_{wall} \approx 2\,\text{s}^{-1}$) and the flow has been steadily imposed for 50 min. As fluid flows from the top towards the bottom of the field of view, the flow becomes focused into the typically observed high-speed jet of the form reported in Fig. 2(b).

Flow profiles of the type shown here have not been reported previously. Ober *et al.*[22] conducted experiments with a CTAB solution of the same formulation as used here and in a microchannel of comparable dimensions, ($w = 1\,\text{mm}$, $d = 130\,\mu\text{m}$). However, measurements were only made of $v_x(z)$ for one value of y ($-0.2 \leq y/w \leq -0.3$), so velocity distributions across the wide channel dimension (i.e., $v_x(y)$) were not ascertained. The reported velocity profiles of $v_x(z)$ evolved from parabolic at low flow rates towards a more plug-like form at higher flow rates, in

qualitative agreement with numerical predictions[22] and with the results of previous authors with strongly shear-thinning and shear-banding fluids.[24,25]

Use of a second rectangular microchannel of dimensions $w = 1.50\,\text{mm}$, $d = 250\,\mu\text{m}$, oriented vertically, permits measurements of $v_x(z)$ for the CTAB solution that can be qualitatively compared to the data of Ober *et al.*[22] For these experiments, a $20\times$ NA $= 0.4$ objective is used for the μ-PIV measurements (measurement depth $\approx 14\mu\text{m}$, or $\approx 0.01w$).[26] The measurement plane is scanned through y in 20 μm increments between the midplane and a side wall, and the data from each plane are stacked to provide the full velocity distribution $v_x(y, z)$ over half of the channel cross-section, as shown in Fig. 6 for two different flow rates. The process of acquiring the full velocity fields in this manner takes up to 1 h, so there is most certainly some smearing of the data due to the time delay between acquisition at different measurement planes. However, it is clear that as the flow rate is increased the velocity distribution over the channel cross-section becomes much more uniform (i.e., plug-like), as expected for this shear-thinning fluid. The startling result is the clear presence of the high velocity jet of fluid observed near the side wall of the channel at the lower flow rate of $Q = 0.069\mu\text{l s}^{-1}$ (Fig. 6(a)). The nominal wall shear rate in this case is $\dot{\gamma}_{wall} \approx 4.4\,\text{s}^{-1}$, which is of very similar magnitude to the shear rates at which these anomalous fluid jets were observed in the previous microchannel (Figs. 3(b) and 3(c)). Obviously, by only making measurements in a single plane (at the position approximately marked by the dashed lines on Fig. 6) Ober *et al.* could not have observed such phenomena in their experiments.[22]

Many questions remain about the origin of the spatio-temporally dependent velocity profiles reported here. It is clear that over a wide range of imposed flow rates, the stress distribution across the width of the channel diverges widely from the predictions of the shear-thinning model, therefore pointing towards an elastic cause for the instability. It is possible that this pressure difference is compensated by normal stresses due to fluid elasticity. On the other hand, the instability is only observed at wall shear rates corresponding to the power-law region of the flow curve (within the low-shear-rate Newtonian plateau of the flow curve the instability is not observed, and approaching the high-shear-rate plateau it is significantly suppressed); this suggests shear-thinning being particularly important as the cause. However, the fact that the GNF model does not reproduce this anomalous
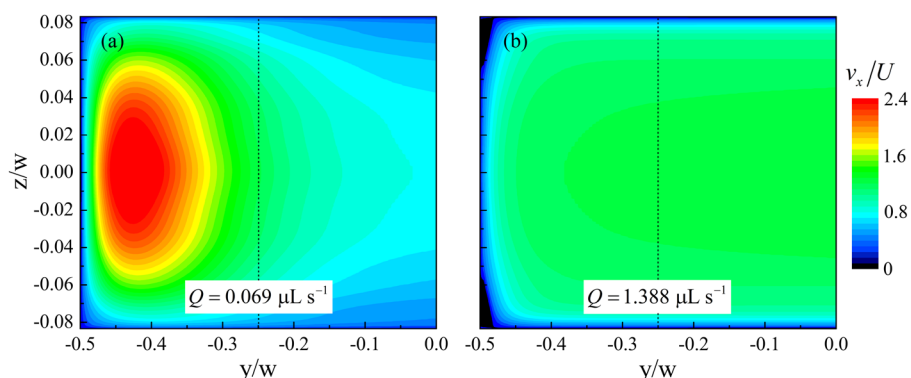

FIG. 6. μ-PIV measurements in the y-z plane of a rectangular microchannel ($w = 1.50\,\text{mm}$, $d = 250\,\mu\text{m}$) at the flow rates indicated on the plots. The corresponding nominal wall shear rates are: (a) $\dot{\gamma}_{wall} \approx 4.4\,\text{s}^{-1}$; and (b) $\dot{\gamma}_{wall} \approx 89\,\text{s}^{-1}$. The flow direction is into the page. The superimposed dashed lines indicate the approximate measurement position used by Ober *et al.*[22]

behavior, suggests a probable coupling between shear-thinning, normal stress, and memory effects. Future attempts to shed light on the problem will initially focus on examining alternative fluids such as shear-thinning but relatively inelastic xanthan gum solutions, and constant viscosity but elastic dilute polymer solutions. This will help to clarify if any particular aspect of the non-Newtonian rheology is at the root. Also interesting will be to examine different wormlike micellar solutions such as the well-studied shear-banding cetylpyridinium chloride CPyCl/NaSal system.[19,20,22,24,27] Ober *et al.*[22] already presented three-dimensional velocimetry data for such a fluid in their rectangular microchannel. There were no abnormalities apparent in their data, but only one particular flow rate was tested, so the results are not necessarily conclusive. It may also be valuable to probe the fluid microstructure within the high velocity and low velocity regions of the microchannel. Flow-induced birefringence measurements may provide an effective qualitative method for doing this.

Notwithstanding the mechanism or reason for the anomalous velocity distributions observed here with the CTAB solution, they clearly have some important consequences. It is normally taken for granted that the flow in such high aspect ratio channels as those used here is essentially two-dimensional, i.e., invariant across the large dimension (w, as it is defined here). It is now clear that this assumption cannot be relied upon for all complex fluids. This has practical implications for the use of high aspect ratio microchannels as microfluidic rheometers.[25,28] It is essential the flow field be fully characterized in such devices over the range of shear rates to be measured if the results obtained are to be properly valid. These phenomena also need to be understood and accounted for in order to optimize industrial processes involving transport and mixing of complex fluids in micro to milli-scale geometries such as those encountered in inkjets, porous media, and lab-on-a-chip devices, for example.

[1]R. G. Larson, *The Structure and Rheology of Complex Fluids* (Oxford University Press, New York, 1999).

[2]J. F. Berret, *Molecular Gels: Materials With Self-Assembled Fibrillar Networks* (Springer, Dordrecht, 2006), pp. 667–720.

[3]S. Ezrahi, E. Tuval, and A. Aserin, Adv. Colloid Interface Sci. **128–130**, 77 (2006).

[4]J. Yang, Curr. Opin. Colloid Interface Sci. **7**, 276 (2002).

[5]J. P. Rothstein, *Rheology Reviews* (The British Society of Rheology, Aberystwyth, 2008), pp. 1–46.

[6]M. E. Cates, J. Phys. Chem. **94**, 371 (1990).

[7]N. A. Spenley, M. E. Cates, and T. C. B. McLeish, Phys. Rev. Lett. **71**, 939 (1993).

[8]R. Makhloufi, J. P. Decruppe, A. Aït-Ali, and R. Cressely, Europhys. Lett. **32**, 253 (1995).

[9]R. Mair and P. T. Callaghan, Europhys. Lett. **36**, 719 (1996).

[10]S. Manneville, Rheol. Acta **47**, 301 (2008).

[11]P. D. Olmsted, Rheol. Acta **47**, 283 (2008).

[12]S. Lerouge and J. F. Berret, Adv. Polym. Sci. **230**, 1 (2010).

[13]M. Vasudevan, E. Buse, D. L. Lu, H. Krishna, R. Kalyanaraman, A. Q. Shen, B. Khomami, and R. Sureshkumar, Nature Mater. **9**, 436 (2010).

[14]N. Dubash, J. Cardiel, P. Cheung, and A. Q. Shen, Soft Matter **7**, 876 (2011).

[15]J. A. Pathak and S. D. Hudson, Macromolecules **39**, 8782 (2006).

[16]M. A. Fardin, D. Lopez, J. Croso, G. Grégoire, O. Cardoso, G. H. McKinley, and S. Lerouge, Phys. Rev. Lett. **104**, 178303 (2010).

[17]P. Nghe, S. M. Fielding, P. Tabeling, and A. Ajdari, Phys. Rev. Lett. **104**, 248303 (2010).

[18]M. A. Fardin, T. J. Ober, C. Gay, G. Grégoire, G. H. McKinley, and S. Lerouge, Europhys. Lett. **96**, 44004 (2011).

[19]S. J. Haward, T. J. Ober, M. S. N. Oliveira, M. A. Alves, and G. H. McKinley, Soft Matter **8**, 536 (2012).

[20]S. J. Haward and G. H. McKinley, Phys. Rev. E **85**, 031502 (2012).

[21]M. A. Fardin, T. J. Ober, C. Gay, G. Grégoire, G. H. McKinley, and S. Lerouge, Soft Matter **8**, 910 (2012).

[22]T. J. Ober, J. Soulages, and G. H. McKinley, J. Rheol. **55**, 1127 (2011).

[23]T. Takahashi, M. Shirakashi, K. Miyamoto, and G. G. Fuller, Rheol. Acta **41**, 448 (2002).

[24]C. Masselon, J.-B. Salmon, and A. Colin, Phys. Rev. Lett. **100**, 038301 (2008).

[25]P. Nghe, G. Degré, P. Tabeling, and A. Ajdari, Appl. Phys. Lett. **93**, 204102 (2008).

[26]C. D. Meinhart, S. T. Wereley, and M. H. B. Gray, Meas. Sci. Technol. **11**, 809 (2000).

[27]H. Rehage and H. Hoffmann, Mol. Phys. **74**, 933 (1991).

[28]C. J. Pipe, T. S. Majmudar, and G. H. McKinley, Rheol. Acta **47**, 621 (2008).

CEFT

Centro de Estudos de Fenómenos de Transporte

Transport Phenomena Research Center